Phononic Frequency Combs in Atomically Thin Nanoelectromechanical Resonators via 1:1 and 2:1 Internal Resonances

S M Enamul Hoque Yousuf, *Graduate Student Member, IEEE*, Jaesung Lee, *Member, IEEE*, Steven W. Shaw, and Philip X.-L. Feng, *Senior Member, IEEE*

***Abstract*— We report on the first experimental demonstrations of phononic frequency comb (PnFC) generation in atomically thin molybdenum disulfide (MoS_2) nanoelectromechanical systems (NEMS) vibrating near ∼20MHz and ∼50MHz in the high frequency (HF) and very high frequency (VHF) bands. Frequency comb patterns are generated by tuning two resonance modes with gate voltage (V_g) to satisfy 1:1 and 2:1 internal resonance conditions. In the 1:1 internal resonance condition, we drive the two modes of a four-layer (4L) MoS_2 NEMS resonator at an anti-crossing in the nonlinear regime, where efficient nonlinear energy transfer occurs between the two coupled modes. The frequency comb characteristics are tunable by varying the RF driving voltage (v_{drv}) and V_g. We find a threshold of PnFC generation at $v_{drv} = 550$mV and $V_g = -6.4$V with relatively wide comb teeth spacing (f_r) around 2.44 to 2.65MHz. In the 2:1 internal resonance condition, pumping a single-layer (1L) MoS_2 NEMS resonator at a frequency twice that of the fundamental mode (f_1) enables mode coupling between f_1 and the mode near $2f_1$, and generates PnFC with tunable f_r. At $V_g = 10$V, pump voltage $v_p = 60$mV, and pump frequency $f_p = 48$MHz, we observe PnFC with f_r ∼45kHz, which can be tuned by varying v_p and f_p. We also demonstrate extraordinarily strong parametric amplification and spectral linewidth narrowing effects in 1L MoS_2 NEMS resonator and achieve parametric gain as high as ∼10,000 (80dB) and spectral linewidth narrowing factor of ∼5000 with $v_p = 153$mV. The PnFCs demonstrated and the findings herein will be valuable for applications such as improving the sensitivity of resonant sensors. [2023-0017]**

***Index Terms*— Phononic frequency comb, 1:1 internal resonance, 2:1 internal resonance, resonators, frequency tuning, nanoelectromechanical systems (NEMS), parametric amplification.**

Manuscript received 8 February 2023; revised 20 March 2023; accepted 2 April 2023. Date of publication 20 June 2023; date of current version 2 August 2023. This work was supported in part by the National Science Foundation (NSF) through the University of Florida under Grant ECCS-2015708, Grant CCF-2103091, and Grant DUE-2142552. The work of Steven W. Shaw was supported in part by the NSF-Binational Science Foundation (BSF) through Florida Tech under Grant 2018041. Subject Editor R. T. Howe. *(Corresponding author: Philip X.-L. Feng.)*

S M Enamul Hoque Yousuf and Philip X.-L. Feng are with the Department of Electrical and Computer Engineering, University of Florida, Gainesville, FL 32611 USA (e-mail: syousuf@ufl.edu; philip.feng@ufl.edu).

Jaesung Lee was with the Department of Electrical and Computer Engineering, University of Florida, Gainesville, FL 32611 USA. He is now with the Department of Electrical and Computer Engineering, The University of Texas at El Paso, El Paso, TX 79968 USA (e-mail: jlee20@utep.edu).

Steven W. Shaw is with the Department of Mechanical and Civil Engineering, Florida Institute of Technology, Melbourne, FL 32901 USA, and also with the Department of Mechanical Engineering and the Department of Physics and Astronomy, Michigan State University, East Lansing, MI 48823 USA (e-mail: sshaw@fit.edu).

Color versions of one or more figures in this article are available at https://doi.org/10.1109/JMEMS.2023.3282233.

Digital Object Identifier 10.1109/JMEMS.2023.3282233

I. Introduction

THE invention of optical frequency combs (OFCs) has provided an elegant method for coherently combining the electromagnetic (EM) spectrum and establishing a bidirectional, coherent link between optics and radio frequency electronics [1], [2]. The unification of the EM spectrum has unlocked vast new capabilities and produced unanticipated breakthroughs. Octave spanning OFCs have enabled novel applications, including precise measurement of optical atomic clocks, frequency comb spectroscopy, arbitrary optical waveform generation and measurement, low noise microwave generation, frequency and time transfer, coherent light detection and ranging (LIDAR), spectrograph calibration and exoplanet search [3], [4], [5], [6], [7], [8], [9].

Following the success and influence of their pioneering optical counterparts, *phononic* frequency combs (PnFCs) are attractive and intriguing as novel devices for mechanical frequency conversion, sensing, and precision measurement, and have recently been demonstrated [10], [11], [12], [13], [14], [15], [16], [17], [18], [19], [20], [21], [22], [23], [24], [25], [26], [27], [28], [29], [30], [31]. A study of two elastically coupled GaAs nanomechanical resonators has revealed amplitude modulated spontaneous oscillation with period doubling transition and chaos in resonators with large vibration amplitude [11]. In piezoelectric microelectromechanical systems (MEMS), PnFCs have been demonstrated utilizing three-wave mixing [14] and nondegenerate parametric driving [18]. Recently, a few PnFCs have been demonstrated by coupling mechanical resonance modes where vibrational energy is coherently transferred back and forth between the coupled modes [16], [27], [31]. Mode coupling becomes strong enough to transfer energy and produces various nonlinear phenomena if the coupled modes have a commensurate frequency relationship (*e.g.*, 1:1, 2:1, and 3:1), known as internal resonance. Therefore, devices with highly tunable frequency and rich nonlinearity are preferred for constructing PnFCs and obtaining internal resonance conditions.

The emergence of two-dimensional (2D) materials such as graphene and molybdenum disulfide (MoS_2) has enabled the development of atomically thin nanoelectromechanical systems (NEMS) [32], [33], [34], [35], [36]. 2D NEMS resonators are extremely sensitive to external perturbations, such as mass, force, pressure, etc., and are opening new avenues for classical and quantum sensing applications. Thanks to their ultrathin suspended structures, these devices often operate

in the membrane regime, where their resonance frequencies are strain-dependent, allowing for extremely broad frequency tuning ranges, up to $\Delta f/f$ ~430% [35]. Electrostatic forces induced by a gate voltage V_g have been widely used to achieve frequency tuning in 2D NEMS, and the resonance frequency can be adjusted to lower or higher values through capacitive softening (at low $|V_g|$) or electrostatic stiffening (at high $|V_g|$, stretching dominates) effects [33], [34], [35]. Due to their extraordinary frequency tunability, 2D NEMS resonators facilitate internal resonance conditions and mode coupling, making them an ideal platform for developing new, tunable PnFCs. However, electrical readout of minuscule resonance motions of these devices is challenging because the intrinsic thermomechanical noise floor is often overwhelmed by noise from the electronics used at the front-end of measurement system. Quality factors (Qs) of 2D resonators can be limited because of various extrinsic damping effects. To increase the signal-to-noise ratio and Qs of 2D resonators, parametric amplification has been proposed to enhance the vibration amplitude at resonance frequency f_1 with pump frequency of $f_p \approx nf_1$, where n is an integer ($n \geq 2$) [37], [38], [39], [40], [41], [42], [43], [44], [45], [46], [47]. Parametric oscillation, also sometimes called self-oscillation, occurs above the threshold pump voltage and does not require any feedback. Thus, parametric oscillation can offer low noise compared to conventional simple electrical oscillator circuit. Recent experiments on photothermal parametric pumping of undriven thermomechanical noise spectra have demonstrated giant parametric amplification with gains up to 71dB and spectral linewidth narrowing factor up to 1.8×10^5 [48]. However, toward on-chip integration of parametric pumping, electrical parametric pumping is desired.

In this work, we utilize electrostatically tunable four-layer (device 1) and single-layer (device 2) MoS_2 NEMS resonators and demonstrate PnFCs generation by employing resonance mode coupling via internal resonance (Fig. 1). By tuning resonance frequencies of two nearby modes at 47.3MHz and 48.1MHz in device 1, the 1:1 mode coupling is achieved. Introducing a single-frequency driving signal around the anti-crossing point of the coupled modes engenders PnFC with comb spacing f_r ~2.44MHz to 2.65MHz, which can be tuned by varying the drive voltage. We demonstrate PnFC in the single-layer (1L) MoS_2 NEMS resonator (device 2) by establishing 2:1 mode coupling via internal resonance and parametrically pumping the resonator at twice frequency of the fundamental mode. We explore the full range of parametric amplification by directly measuring and pumping the intrinsic thermomechanical noise. We experimentally demonstrate parametric gain up to ~10,000 (80dB) before the device goes into parametric self-oscillation. The exceptional linewidth narrowing factor of ~5000 reveals the efficient electrical pumping in the sub-threshold regime (before self-oscillation). Next, we experimentally demonstrate a PnFC generation near the fundamental mode (f_1) by pumping near the 3rd mode ($f_3 \approx 2f_1$) that satisfies 2:1 mode coupling. The comb spacing and number of teeth can be tuned by varying the pump voltage and frequency.

II. Device Design and Fabrication Process

To demonstrate PnFCs, we design and fabricate electrostatically tunable circular drumhead MoS_2 NEMS resonators with a local gate configuration by using multiple photolithography and etching steps compatible with standard MEMS fabrication processes (Fig. 2a-2e). We use a 4-inch insulating sapphire wafer as the substrate to reduce undesired and unwanted RF signal crosstalk. To enable the local electrostatic gate control, we pattern 23nm Pt on 2nm Ti followed by 300nm SiO_2 deposition using plasma enhanced chemical vapor deposition (PECVD) technique. To improve the oxide quality and minimize the defects in the oxide layer, we deposit 20nm Al_2O_3 using atomic layer deposition (ALD). Next, we form 290nm deep circular microcavities using reactive ion etching (RIE). We use another photolithography step to deposit metals (200nm Au on 5nm Ti) to form contact pads and electrodes. Finally, we dry-transfer an exfoliated MoS_2 flake using polydimethylsiloxane (PDMS) on the prepatterned electrodes and cavity to form suspended circular drumhead resonator. We fabricate device 1 (4L MoS_2) with $d = 2\mu$m and device 2 (1L MoS_2) with $d = 3\mu$m to demonstrate PnFCs using 1:1 and 2:1 internal resonances, respectively.

III. Measurement Techniques

A. 2D Material Characterization on NEMS Platform

Following device fabrication, Raman spectroscopy and photoluminescence (PL) measurements are used to extract the number of layers in the suspended MoS_2 flakes. We use a green laser (wavelength $\lambda = 532$nm) to measure Raman and PL signals. Figure 2f and 2g show the acquired Raman and PL spectra for the suspended MoS_2 flake of the 4L device. The suspended flake exhibits a prominent in-plane Raman mode at $E^1_{2g} = 384.75\text{cm}^{-1}$ and out-of-plane Raman active mode at $A_{1g} = 408.70\text{cm}^{-1}$ with peak separation 23.95cm^{-1}, confirming the signature of 4L MoS_2 in the suspended region over the cavity [49]. The obtained PL spectrum shows a strong indirect band transition at 900nm, confirming that the suspended MoS_2 membrane in device 1 has 4L MoS_2. We also observe a strong sharp peak at ~694nm due to emission from the sapphire substrate. The single-layer (1L) nature of the MoS_2 flake in device 2 is confirmed from prominent Raman peaks at $E^1_{2g} = 385.44\text{cm}^{-1}$ and $A_{1g} = 403.65\text{cm}^{-1}$ with peak separation 18.21cm^{-1}. Thanks to direct exfoliation from the bulk crystal, all the suspended flakes exhibit high-quality crystallinity as confirmed from Raman and PL spectra.

B. Optical Interferometry Measurement System

We utilize a custom-built laser interferometry system (Fig. 3) to measure and characterize the performance of the NEMS resonators. A $\lambda = 632.8$nm He-Ne red laser is focused onto the suspended MoS_2 circular drumhead using a 50× microscope objective. The red laser power on the suspended flake is limited below 300μW to avoid excess laser heating. The estimated spot size of the red laser is ~1μm. The reflected red laser is modulated by the vibrational motion of the suspended membrane and is collected by a

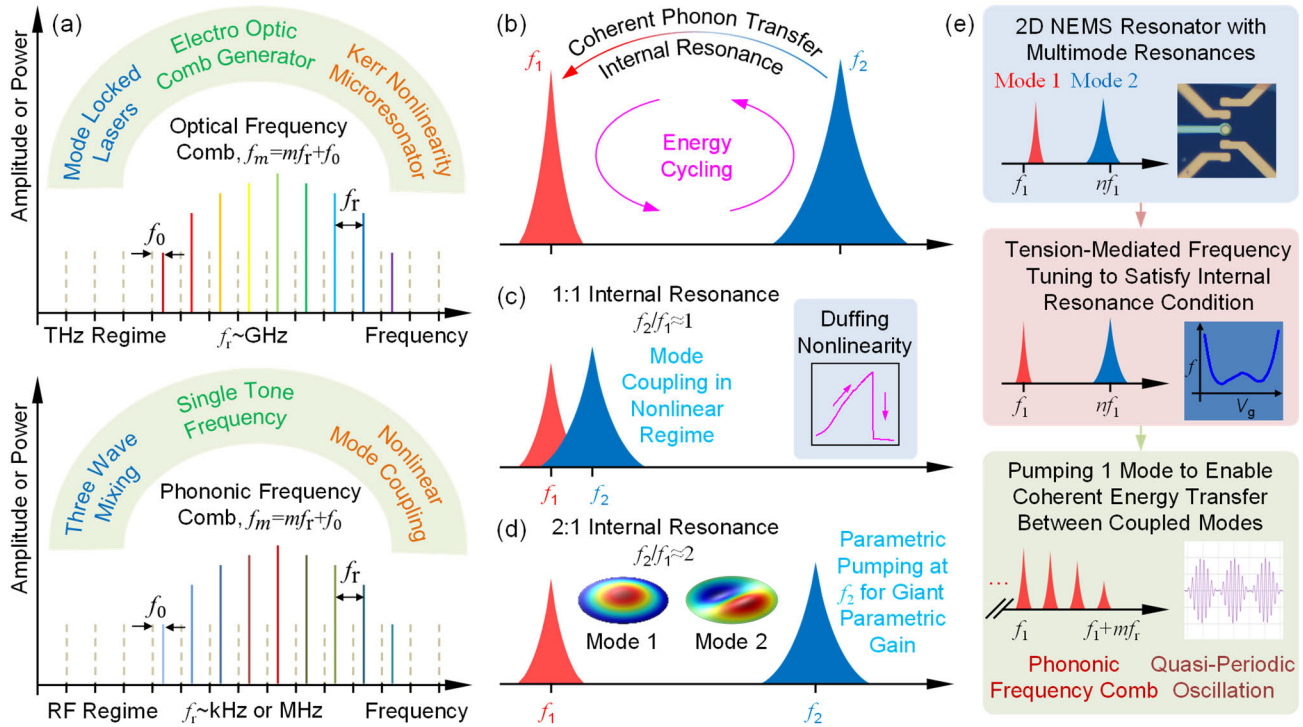

Fig. 1. Conceptual illustration of phononic frequency comb (PnFC) generation in atomically thin 2D NEMS resonators. (a) Optical frequency comb (OFC) and phononic frequency comb (PnFC) generation in the THz and MHz regimes, respectively, by employing different techniques. m: integer mode number. (b) Energy cycling in two different modes with commensurate frequency relationship enables coherent phonon transfer and establishes internal resonances. (c) 1:1 and (d) 2:1 mode coupling and internal resonance with $f_2/f_1 \approx 1$ and $f_2/f_1 \approx 2$, respectively. (e) Illustration of phononic frequency comb generation by tuning the resonance modes via tension to satisfy mode coupling and internal resonance condition. Pumping one mode enables coherent energy transfer and generates quasi-periodic oscillation in time domain which corresponds to a phononic frequency comb in the frequency domain.

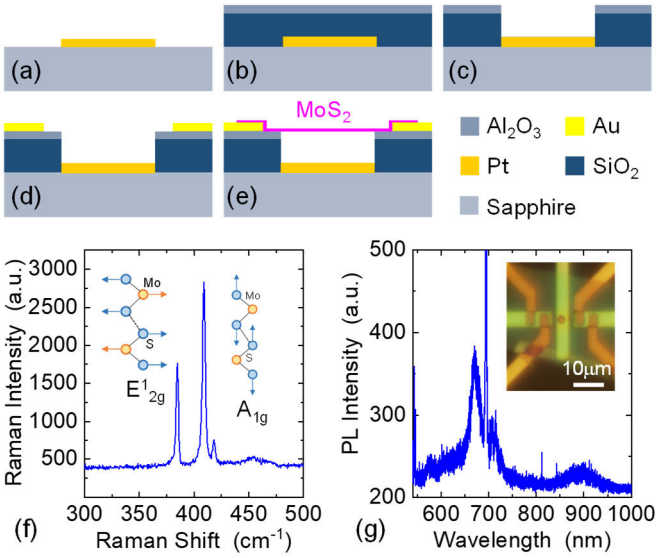

Fig. 2. Fabrication process of the MoS_2 drumhead resonators. (a) Local gate patterning on the bare sapphire substrate. (b) 300nm SiO_2 and 20nm Al_2O_3 deposition. (c) Reactive ion etching (RIE) to form 290nm-deep trench. (d) Metal deposition to form top electrodes. (e) All-dry transfer of the selected MoS_2 flake to make suspended resonator. (f) Raman signal showing E^1_{2g} and A_{1g} modes at 384.75cm^{-1} and 408.70cm^{-1}, respectively for the 4L device. (g) Photoluminescence spectra from the suspended region of the device. *Inset*: Optical image of the 4L device with diameter $d \approx 2\mu$m.

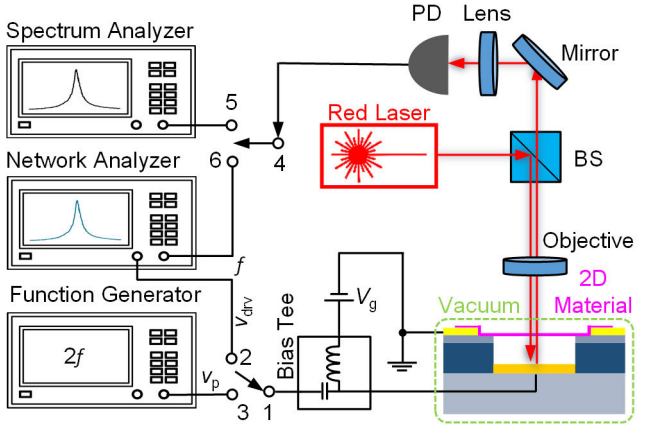

Fig. 3. Illustration of the measurement scheme showing the techniques for detecting undriven thermomechanical noise (connect nodes 4,5) and driven resonances (connect nodes 1,2 and 4,6). A function generator is used for parametrically pumping the devices (connect nodes 1,3) and the corresponding spectrum is observed using a spectrum analyzer (connect nodes 4,5). Red laser (wavelength $\lambda = 632.8$nm) is used to probe the displacement of the vibrating membrane. BS: beam splitter, PD: photodetector.

photodetector, which converts the optical signal to electrical signal. A spectrum analyzer is used to monitor and record the undriven thermomechanical noise spectrum. To measure the driven resonance, RF signal from a network analyzer is combined with DC gate voltage using a bias tee and applied to the local gate. In the driven resonance case, the electrical signal from the photodetector is recorded using the same network analyzer. For parametric resonance characterization, electrical pump signal $(2f_1)$ is introduced at the local gate from a function generator and the corresponding spectra is recorded using the spectrum analyzer. PnFCs are generated in the RF regime by introducing a single drive frequency at the

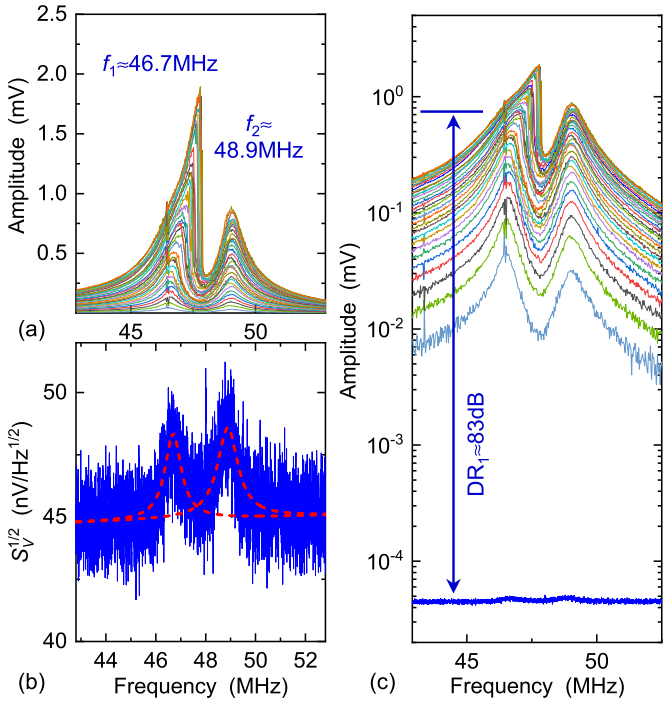

Fig. 4. Resonance characterization of the 4L device at $V_g = -3$V. (a) Driven resonance at varying v_{drv} from 10mV to 300mV with 10mV step. (b) Measured thermomechanical noise showing two modes. (blue curve: experimental data, red curves: fitting). (c) Log plot of the measured undriven thermomechanical noise and driven resonance shows DR_1 ≈83dB for mode 1.

local gate from a function generator and the signal is recorded by using the spectrum analyzer. All measurements are carried out at room temperature (T ≈300K) and in moderate vacuum (p ≈20mTorr).

IV. Dynamic Range and Frequency Tuning of Device 1

We achieve 1:1 mode coupling and internal resonance condition between two nearby modes in device 1 with 4L suspended MoS_2 membrane (Fig. 4). We study the undriven and driven resonance, Duffing nonlinearity, and dynamic range (DR) of the 2D NEMS resonator to characterize and calibrate the two modes and determine the necessary conditions to achieve internal resonance. Without applying any RF drive (v_{drv}), we measure undriven thermomechanical noise with fixed $V_g = -3$V. The resonance frequency f_n and quality factor Q_n of n^{th} mode can be extracted by fitting to a simple harmonic resonator model to describe the thermomechanical motion of a resonator expressed as [32]

$$S_{x,\mathrm{th},n}^{1/2} = \left(\frac{4k_B T \omega_n}{m_{\mathrm{eff},n} Q_n} \cdot \frac{1}{\left(\omega^2 - \omega_n^2\right)^2 + \left(\omega\omega_n / Q_n\right)^2} \right)^{\frac{1}{2}}. \quad (1)$$

Here, k_B, T, ω_n, and $m_{\mathrm{eff},n}$ represent Boltzmann's constant, temperature, angular resonance frequency, and effective mass of the n^{th} mode, respectively. By fitting the experimental data to Eq. (1), we obtain two resonance modes at $f_1 = 46.7$MHz with Q_1 ≈60, and $f_2 = 48.9$MHz with Q_2 ≈50 (Fig. 4b). To measure the driven resonance, we combine v_{drv} from the network analyzer with DC gate voltage $V_g = -3$V using a bias tee and apply to the local gate. We gradually increase v_{drv} to investigate the nonlinearity and DR of the resonance modes. Clear bifurcation is detected for the first mode under high RF drive, demonstrating stiffening Duffing nonlinearity. DR is defined by the ratio of the signal amplitude at the onset of nonlinearity, also known as 1dB compression point, to the thermomechanical noise floor and expressed as (in dB) [50]

$$DR = 20\log\left(\frac{0.745a_c}{\sqrt{2S_{x,\mathrm{th}}\Delta f}}\right), \quad (2)$$

where a_c is the critical amplitude and $\Delta f = 1$Hz is the measurement bandwidth. For the 1st mode, we observe a dynamic range DR_1 ≈83.5dB. However, the signal amplitude of the 2nd mode keeps increasing without displaying any clear Duffing nonlinearity even at $v_{drv} = 300$mV, indicating DR_2 >85dB (Fig. 4c).

The resonance frequencies of the 2D NEMS resonators are highly tunable and can be leveraged to achieve internal resonances with commensurate frequency relationship. To achieve a 1:1 internal resonance condition, we study the resonance frequency tuning of the drumhead via the local electrostatic gate. We fix the RF drive $v_{drv} = 10$mV to operate the resonator in linear regime and sweep V_g from −20 to 20V with 0.5V step. With the application of V_g at the local gate, the membrane is stretched towards the gate due to electrostatic force and thus the tension in the membrane increases with increased V_g. However, increased V_g also introduces capacitive softening which reduces the resonance frequency. Thus, the frequency tuning of the drumhead resonator depends on the interplay between the V_g-induced elastic stiffening and capacitive softening effect. This can be expressed by [33], [34], Eq. (3), as shown at the bottom of this page, where E_Y, ε_r, ρ, r, h, z_0, and ϵ_0 represent Young's modulus of the material of the membrane, total radial strain due to stretching of the membrane, 3D mass density, radius of the drumhead, thickness of the membrane, depth of the air gap (trench depth), and permittivity of free space. Depending on the initial device parameters, such as built-in tension and vacuum (or air) gap between the suspended membrane and the local gate of the resonator, the combined effect can lead to 'W' or 'U' shaped frequency tuning curves [33], [34], [35].

As we vary V_g, the 4L MoS_2 device exhibits both frequency tuning characteristics (Fig. 5). As we vary V_g from −20V to 20V, the resonance frequency f_1 increases from ∼47MHz to ∼64MHz, providing a frequency tunability $\Delta f_1/f_1$ ≈36% and displays a 'U' shaped resonance frequency tuning curve. On the other hand, f_2 stays close to 50MHz for V_g close to 0V

$$f_1 = \frac{1}{2\pi}\sqrt{\frac{\epsilon_0^2 V_g^4}{2.156\left(1-\nu^2\right)E_Y h^2 \varepsilon_r^2 \rho z_0^4} + \frac{2.4^2 E_Y \varepsilon_r}{\rho r^2} - \frac{\epsilon_0}{0.813\rho h z_0^3}V_g^2}, \quad (3)$$

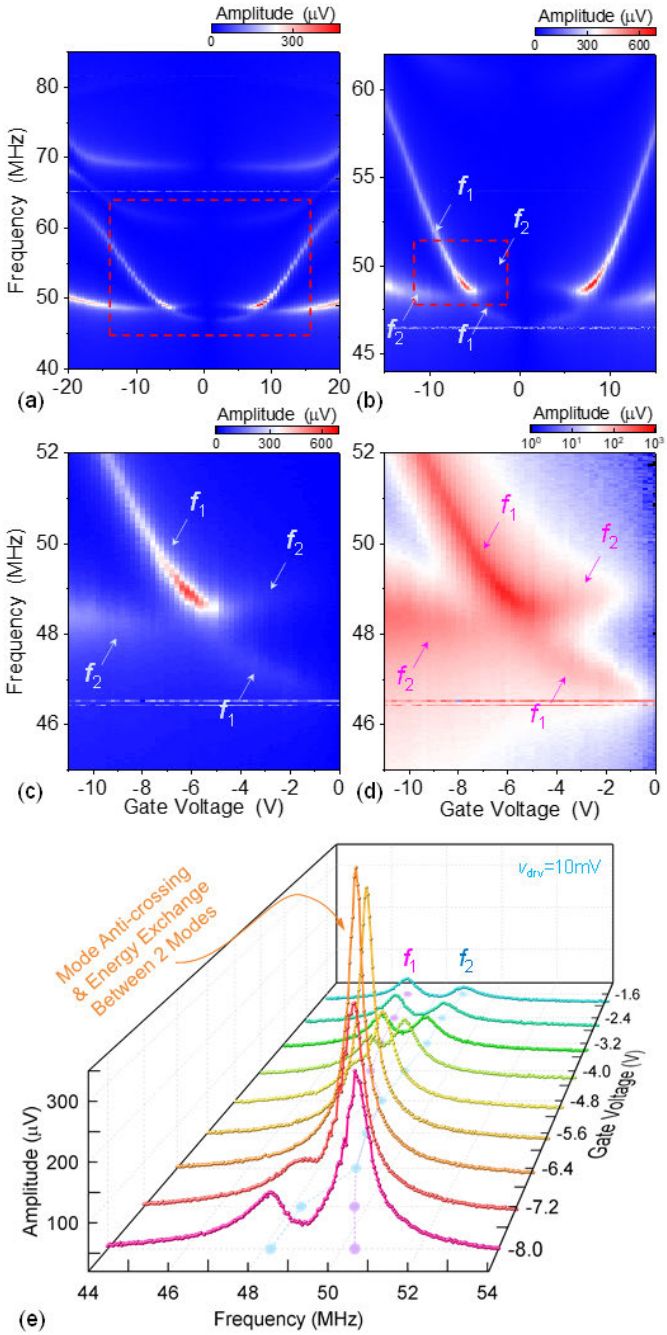

Fig. 5. Resonance frequency tuning of multimode MoS_2 resonator (device 1). (a) 2D color plot of the frequency tuning by varying the gate voltage from −20V to 20V with 0.5V step. Mode 1 (f_1) and mode 2 (f_2) show "U" and "W" shaped frequency tuning curves, respectively. (b) A zoomed-in view of the frequency tuning curves highlighted in red box in (a) with finer gate voltage step (0.2V). (c) Zoomed-in view of the frequency tuning curves highlighted in red box in (b). (d) The signal amplitude in (c) is converted to log scale, showing an anti-crossing point between the frequency tuning curves of f_1 and f_2. (e) Evolution of mode 1 and mode 2 by varying $V_g = -8$V to −1.6V, clearly showing the mode anti-crossing point near $V_g = -6$V.

and reduces to ∼48MHz at $V_g = \pm 10$V. However, f_2 increases again and shifts to ∼50MHz at $V_g = \pm 20$V, exhibiting a 'W'-shaped frequency tuning curve. The different responses of the resonance frequencies with varying V_g lead to anti-crossing between 1st and 2nd modes near $V_g \approx -6$V to −7V. Near the anti-crossing point, the lower energy branch switches from f_1 to f_2 as we increase $|V_g|$. The upper energy branch, on the other hand, changes from f_2 to f_1 as the resonator response goes through the anti-crossing point. Figure 5e shows a set of resonance response curves by varying $V_g = -8$V to −1.6V with 0.8V step. At lower $|V_g|$, two distinct modes are clearly visible. As we increase $|V_g|$, the modes get closer to each other and at the anti-crossing point, they exchange energy. Response curves clearly shows the transition between f_1 and f_2 near $V_g = -6.4$V.

V. Phononic Frequency Comb via 1:1 Internal Resonance and Mode Coupling

The essential governing equations of motion for the 1:1 internal resonance, including Duffing nonlinearity and mode coupling coefficient between two modes can be written as

$$m_{\text{eff},1}\ddot{x}_1 + m_{\text{eff},1}\omega_1\dot{x}_1/Q_1 + k_{1,1}x_1 + k_{3,1}x_1^3 + \eta x_1 x_2^2 = F_1\cos(\omega t), \quad (4)$$

$$m_{\text{eff},2}\ddot{x}_2 + m_{\text{eff},2}\omega_2\dot{x}_2/Q_2 + k_{1,2}x_2 + k_{3,2}x_2^3 + \eta x_2 x_1^2 = F_2\cos(\omega t), \quad (5)$$

where the subscripts 1 and 2 denote mode 1 and mode 2, respectively, and η is the nonlinear coupling coefficient between two modes. Since energy transfer between coupled modes takes place in the nonlinear regime, we characterize the nonlinear dynamics of the MoS_2 resonators focusing on the 1:1 internal resonance condition. Based on the frequency tuning maps shown in Fig. 5c and 5d, V_g is set to be −6.4V, and resonance characteristics are measured with varying v_{drv}. At this 1:1 internal resonance setting, we find f_1 ≈47.3MHz with Q_1 ≈100 and f_2 ≈48.1MHz with Q_2 ≈50 from the thermomechanical noise measurement, showing a frequency splitting of 0.8MHz. Next, we introduce v_{drv} = 5mV to 800mV to the gate with a 15mV step to excite the resonance motion. Figure 6a shows evolution of the resonance with varying v_{drv}. As v_{drv} increases, the peak point shifts upward in frequency, showing an asymmetric resonance shape (*i.e.*, stiffening Duffing nonlinearity). Even at very high v_{drv}, the resonance appears only weakly nonlinear, and the onset of the nonlinearity could be much higher than the measured amplitude. By comparing the measured amplitude at v_{drv} = 800mV with the noise floor, we estimate a measured dynamic range $DR_1 \geq$ 102dB. The surprisingly broad *DR* may be attributed to partial cancellation of opposite Duffing nonlinearity induced by stiffening and capacitive softening, which delays the onset of nonlinearity (Fig. 6c). Moreover, the results indicate the MoS_2 device possesses excellent *DR* tuning, over 19dB, by controlling V_g. The extracted Duffing coefficient k_3 of mode 1 is 5.69236×10^{12} N·m^{-3}.

We now turn our focus to PnFC generation in the MoS_2 NEMS resonator by employing the 1:1 internal resonance mode coupling (Fig. 7a). A single frequency driving signal f_{drv} = 48.06MHz near the anti-crossing is applied to the gate with $V_g = -6.4$V and PnFC spectrum is monitored by using the spectrum analyzer. No clear PnFC pattern is generated when v_{drv} <550mV (Fig. 7a). Upon v_{drv} >550mV, equally spaced comb teeth appear near f_{drv}, showing PnFC. As the coupled modes start to be weakly nonlinear at v_{drv} = 550mV (Fig. 6a), the PnFC appears to be related to nonlinearity of

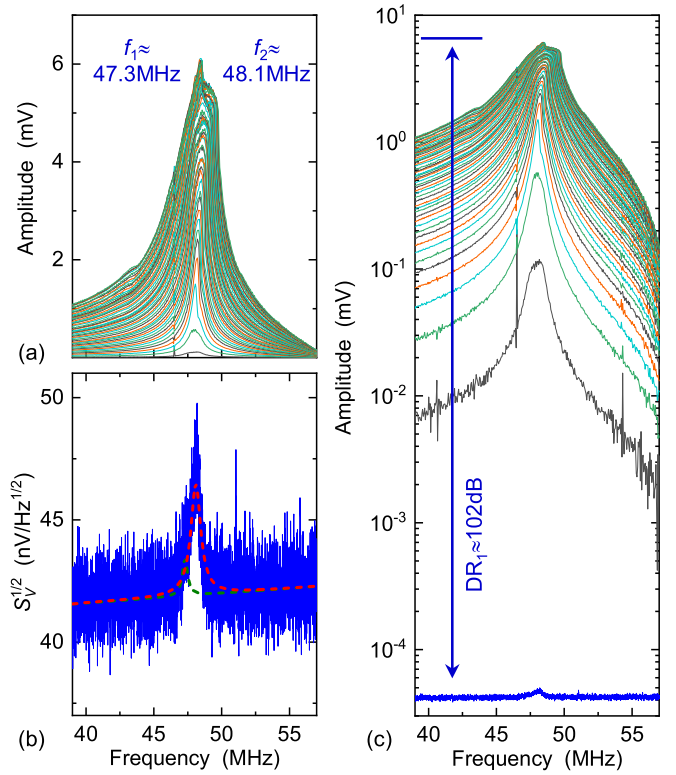

Fig. 6. Measured nonlinearity and dynamic range of the 4L MoS_2 NEMS resonator at $V_g = -6.4$V. (a) Progression of driven resonance with varying v_{drv} from 5mV to 800mV with 15mV step showing the Duffing nonlinearity of mode 1. (b) Undriven thermomechanical noise measurement from the device showing two resonance modes. The fitted curves (cyan and red dashed lines) show two distinct modes(c) Dynamic range measurement by combining the data from (a) and (b) in log scale.

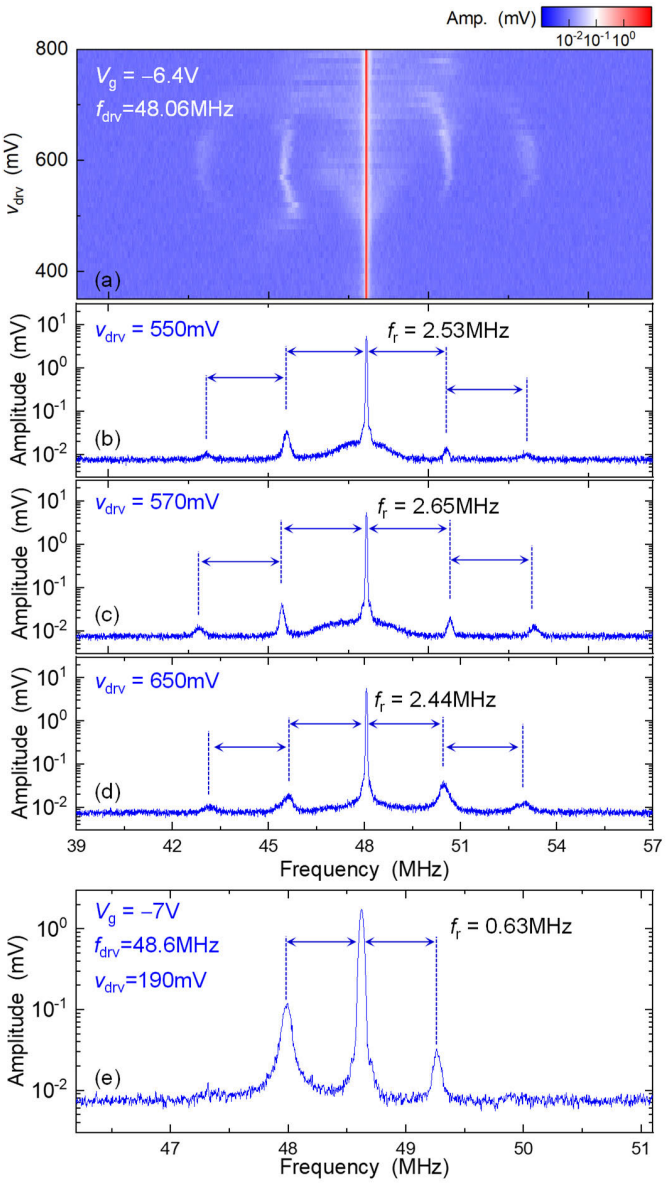

Fig. 7. Phononic frequency comb generation via 1:1 internal resonance. (a) Evolution of phononic frequency comb structure by varying v_{drv} with fixed $V_g = -6.4$V and $f_{drv} = 48.06$MHz. Frequency-domain response of the resonator at (b) $v_{drv} = 550$mV, (c) $v_{drv} = 570$mV, and (d) $v_{drv} = 650$mV showing clear comb structure with comb spacing $f_r = 2.53$MHz, 2.65MHz, and 2.44MHz, respectively. (e) Phononic frequency comb with $V_g = -7$V, $v_{drv} = 190$mV, and $f_{drv} = 48.6$MHz with comb spacing $f_r = 0.63$MHz.

the coupled modes. Initially, the measured comb spacing is $f_r = 2.53$MHz at $v_{drv} = 550$mV (Fig. 7b); it increases to $f_r = 2.65$MHz at $v_{drv} = 570$mV (Fig. 7c) and then decreases to $f_r = 2.44$MHz at $v_{drv} = 650$mV (Fig. 7d). The ratio between PnFC spacing and driving frequency $f_r/f_{drv} = 0.055$, is much higher than those in PnFCs with much larger MEMS resonators ($f_r/f_{drv} \approx 10^{-6} \sim 10^{-3}$) [14], [16]. In the range of $v_{drv} > 700$mV, the PnFC pattern gradually disappears as the amplitudes of the comb teeth becomes smaller.

We also investigate the characteristics of the PnFC at different V_g. At $V_g = -7$V with $f_{drv} = 48.62$MHz and $v_{drv} = 190$mV, a PnFC pattern emerges with $f_r = 0.63$MHz (Fig. 7e). Compared with the PnFC patterns demonstrated at $V_g = -6.4$V, this has narrower frequency spacing. This further shows the strong tunability of the PnFC with varying V_g and thus the resonance mode coupling between two modes of the resonator.

VI. Resonance Characterization of Device 2

To study parametric amplification, we design and fabricate a single-layer (1L) MoS_2 NEMS resonator with diameter $d = 3\mu$m. To characterize the resonator, we first excite the device by applying a $V_g = 10$V gate voltage and $v_{drv} = 3$mV RF drive to the local gate and measure 4 driven resonance modes at 24.4MHz, 37.9MHz, 50.4MHz, and 90.7MHz, with Qs of 170, 138, 107, and 73, respectively (Fig. 8). The signal amplitude of the driven modes gets smaller as we move to the higher modes. To measure the frequency tunability, we fix v_{drv} at 3mV and increase V_g from 0V to 18.5V with 0.1V step, and mode 1 shows clear frequency tuning with varying V_g. Capacitive softening dominates up to $V_g \approx 13$V showing a resonance frequency downshift to 23.58MHz; tension-induced stiffening dominates when $V_g > 13$V, exhibiting frequency upshift to 25.69MHz at $V_g = 18.5$V. Thus, the device shows a 'W' shaped frequency tuning curve for mode 1 with frequency tunability $\Delta f_1/f_1 \approx 9\%$ and provides a tuning knob to satisfy internal resonance condition for efficient energy transfer between coupled modes.

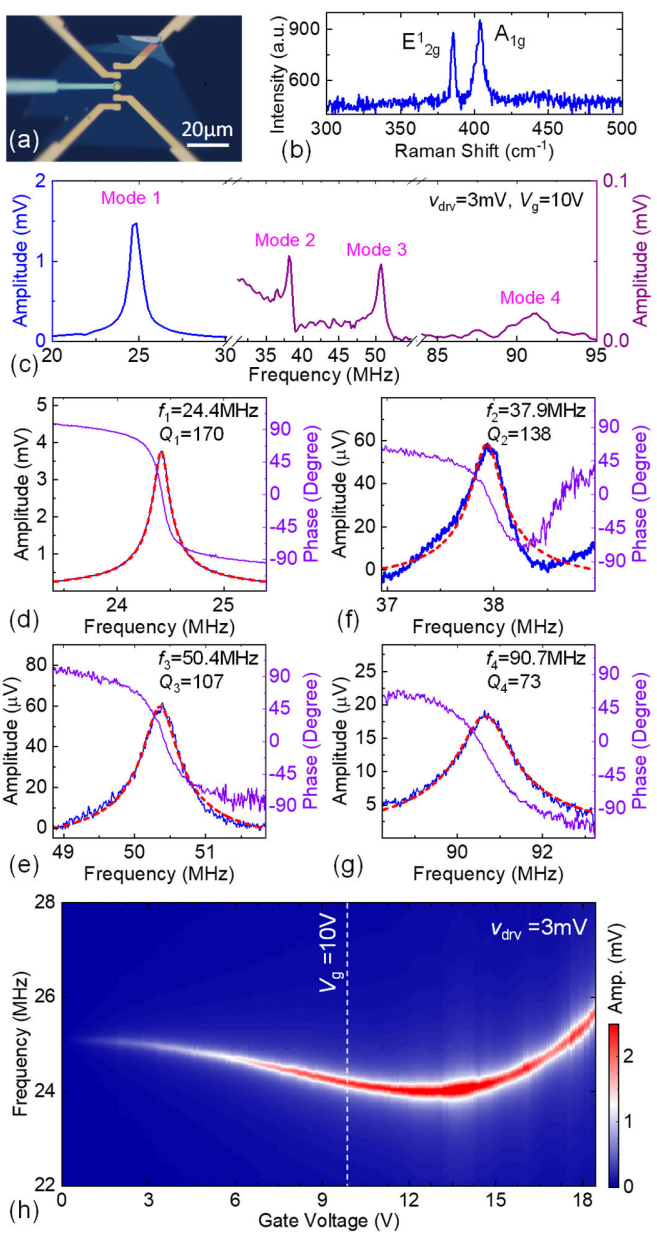

Fig. 8. Resonance characterization of a single-layer (1L) MoS_2 NEMS resonator. (a) Optical image of the fabricated 1L MoS_2 drumhead resonator. Scale bar: 20μm. (b) Confirming the single-layer thickness of the 2D membrane using two prominent E^1_{2g} and A_{1g} Raman peaks at 385.44cm^{-1} and 403.65cm^{-1}, respectively. (c) Measured multimode resonances of the device. Measured driven resonances of the (d) 1st, (e) 2nd, (f) 3rd, and (g) 4th mode using optical interferometry with Qs of 170, 138, 107, and 73, respectively. Blue curves represent experimental data and red dashed curves are obtained from fitting to the damped harmonic resonator model. (h) Tuning of resonance frequency of the first mode by varying V_g from 0 to 18V with fixed v_{drv} = 3mV. The resonator shows a frequency tenability of 9%.

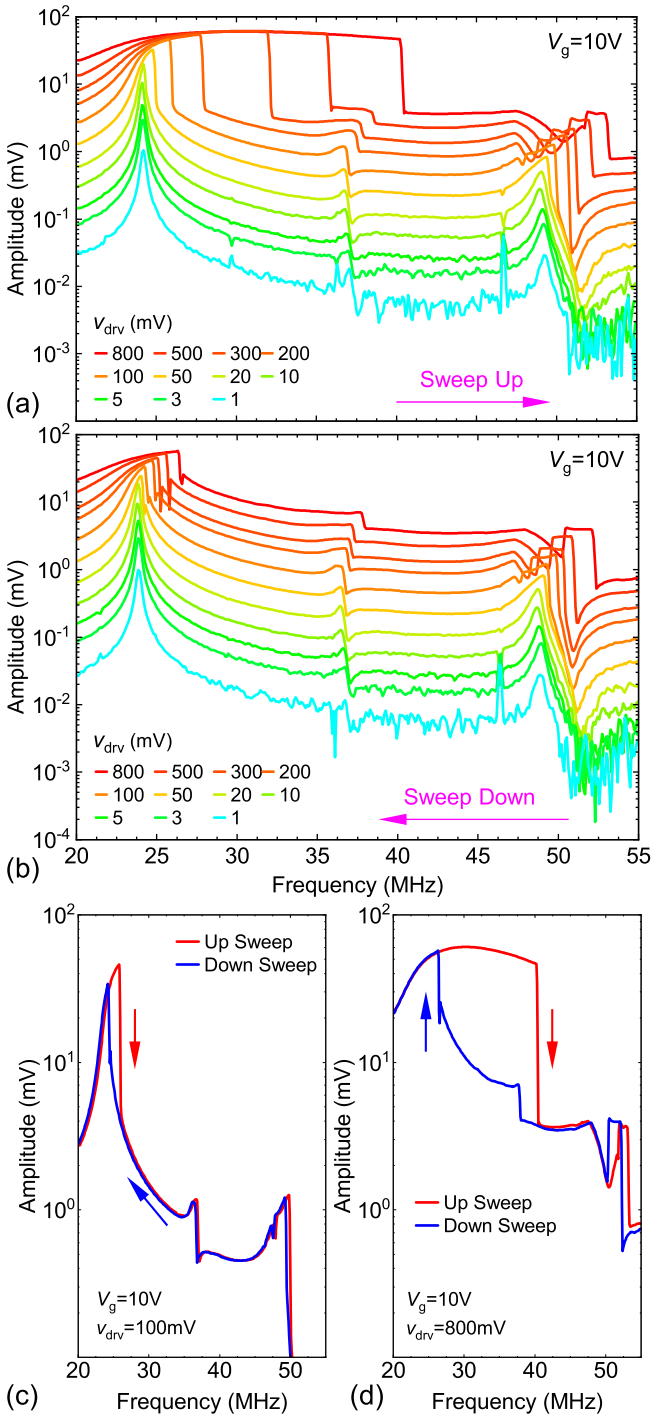

Fig. 9. Duffing nonlinearity measurement. (a) Duffing response measured by varying v_{drv} with fixed V_g = 10V. Each curve was recorded by sweeping the RF drive frequency of the network analyzer from 20MHz to 55MHz (up sweep). (b) Nonlinearity measurement by sweeping the drive frequency of the network analyzer from 55MHz to 20MHz (down sweep) with same condition as in (a). (c) Nonlinear responses at v_{drv} = 100mV shows hysteresis during up (red arrow) and down (blue arrow) sweeps. (d) Clear hysteresis behavior at v_{drv} = 800mV during up and down sweeps. The hysteresis increases from 1.4MHz at v_{drv} = 100mV to 13.9MHz at v_{drv} = 800mV.

Next, we investigate the device response under high v_{drv}. As we increase v_{drv}, the peak frequency increases, and the device goes into the nonlinear regime. The data in Fig. 9 clearly demonstrates Duffing nonlinearity with frequency stiffening effect caused by the membrane tensioning. Therefore, stiffening nonlinearity due to membrane tensioning dominates any possible softening effects present in the device [51]. We also observe hysteresis when we sweep the drive frequency from the network analyzer in opposite directions (up and down sweeps). Frequency hysteresis increases from 1.4MHz at v_{drv} = 100mV to 13.9MHz at v_{drv} = 800mV.

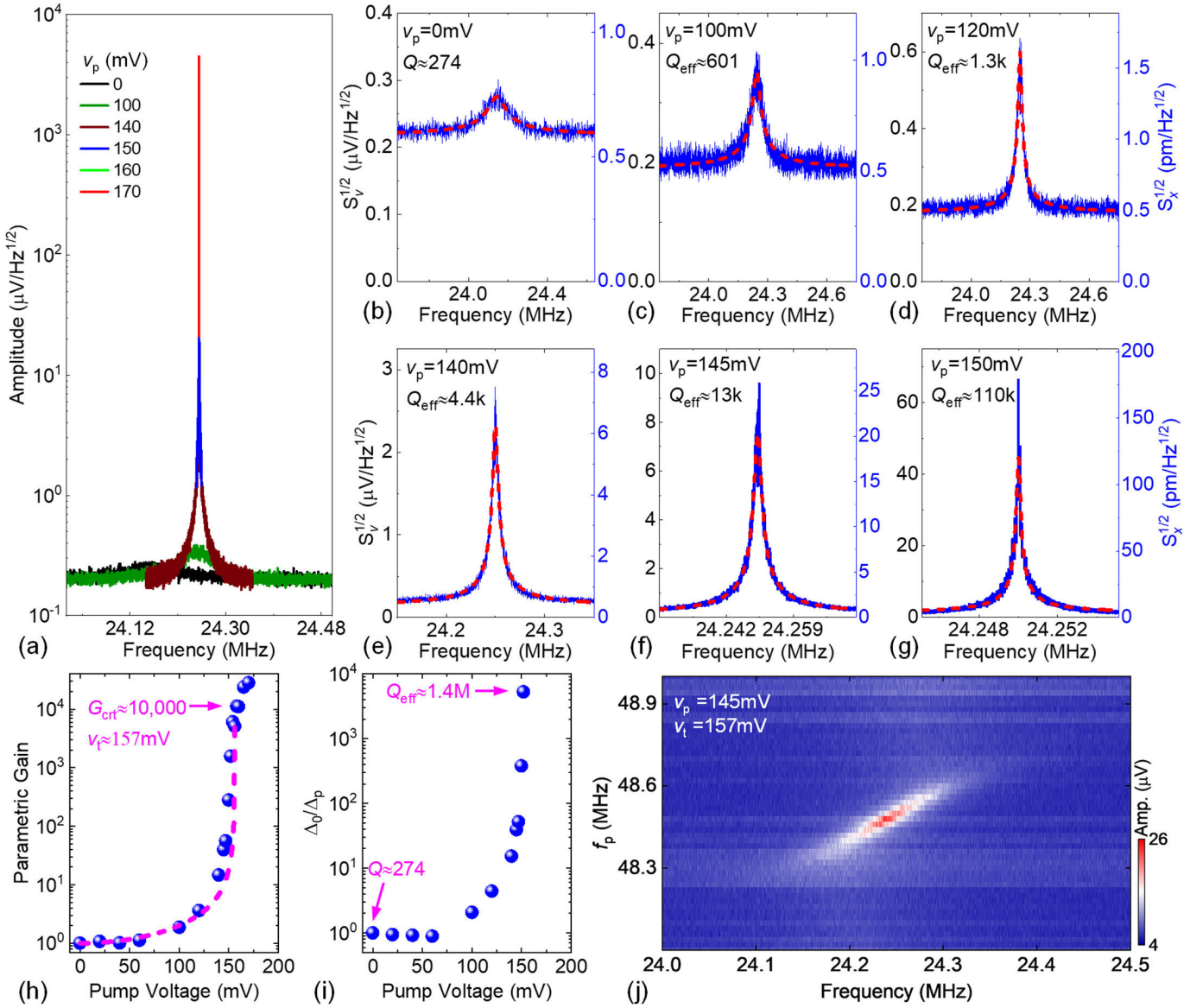

Fig. 10. Degenerate parametric amplification of the undriven thermomechanical noise of the resonator. (a) Measured thermomechanical noise of the single-layer MoS_2 device at varying parametric pump voltage. (b) Measured thermomechanical noise without pumping the device. Thermomechanical noise spectral density with (c)100mV, (d) 120mV, (e) 140mV, (f) 145mV, and (g) 150mV electrical parametric pump voltage introduced at the local gate of the NEMS resonator. Red dashed curves are acquired by fitting the experimentally measured data depicted in blue curves. (h) Extracted parametric gain and (i) spectral linewidth narrowing factor at varying pump voltages. (j) Color plot showing thermomechanical noise measured with varying f_p with fixed pump voltage at 145mV.

VII. Investigation of Parametric Amplification

Resonance motion of the 2D NEMS resonator under local-gate electrical parametric pumping can be described by

$$m_{\text{eff},1}\ddot{x}_1 + \frac{m_{\text{eff},1}\omega_1\dot{x}_1}{Q_1} + \left[k_{1,1} + k_p\cos\left(2\omega_1 t\right)\right]x_1 + k_{3,1}x_1^3 = F\left(t\right), \quad (6)$$

where x_1, t, $m_{\text{eff},1}$, ω_1, $k_{1,1}$, $k_{3,1}$, and $F(t)$ are displacement, time, effective mass, angular frequency at resonance ($\omega_1 = 2\pi f_1$), linear spring constant, third order spring constant, and driving force, respectively. $F(t)$ can be either a harmonic drive with amplitude proportional to RF drive voltage v_{drv} at frequency f_{drv} or thermal noise. The periodic modulation of linear stiffness at $2f_1$ is described by $k_p\cos(2\omega_1 t)$, where k_p indicates the electrical pump strength. In the ideal membrane limit, the resonance frequency of a drumhead depends on the built-in tension γ [N/m], thickness h, and diameter d, and is expressed by

$$f_n = \frac{(\kappa d/2)}{\pi d}\sqrt{\frac{\gamma}{\rho h}}. \quad (7)$$

Here, $\kappa d/2$ is a modal parameter and for the fundamental mode of a circular drumhead, $\kappa d/2 = 2.404$. The resonance frequency can be tuned by varying V_g as described in Eq. (3). We electrically pump the 1L MoS_2 resonator at twice the fundamental mode frequency using a function generator and record the corresponding spectrum. To date, most of the reported parametric MEMS/NEMS resonators have utilized the tension modulation to achieve parametric

TABLE I
BENCHMARKING OF PHONONIC FREQUENCY COMBS IN MEMS/NEMS

Refs	Material	Thickness	Operating Frequency	Teeth Spacing	No of Comb Teeth
This Work	MoS_2	2.8nm	48.06MHz	2.44MHz	5
This Work	MoS_2	0.65nm	24.00MHz	26-45kHz	15
[20]	Graphene	0.34nm	2.87MHz	28.7kHz	16
[27]	Graphene	14nm	22.73MHz	680kHz	9
[24]	MoS_2	1nm	12.20MHz	-	-
[54]	MoS_2	4.55nm	7.7MHz	220kHz-640kHz	7
[12]	GaAs	1.35μm	280kHz	0.01-10Hz	48
[28]	SiN	0.1μm	6.528MHz	1.1kHz	12
[14]	AlN/Si	11μm	3.86MHz	2.6kHz	9
[18]	AlN/Si	-	8.91MHz	70-90kHz	11
[16]	Si	25μm	62.97kHz	-	21
[17]	Si	20μm	26kHz	0.8-2.6kHz	25
[23]	Si	11μm	3.83MHz	9.33kHz	13
[31]	Si	10μm	417kHz	0.103kHz	27

amplification [37], [39], [40], [42], [43], [44]. Atomically thin MoS_2 2D drumheads with low linear stiffness (k_1) [51], [52] operating in the tension-dominated regime provide an ideal testbed for parametric amplification and can be efficiently pumped with electrical pump signal via the local gate.

We measure the thermomechanical noise of the undriven resonator to study the parametric amplification. The measured thermomechanical noise for mode 1 shows a resonance frequency $f_1 = 24.14$MHz with $Q_1 \approx 274$. The responsivity of the system, defined as the ratio of the voltage domain thermomechanical noise spectral density $S_v^{1/2}$ to displacement domain thermomechanical noise spectral density $S_{th}^{1/2}$, is 0.371μV/pm at room temperature. We calculate the displacement of the undriven thermomechanical mode to be 0.15pm without parametric amplification. We also convert the voltage domain measurement to displacement domain by utilizing the responsivity of the system. After characterizing the undriven resonance of the drumhead, the modulation depth of the electrical pumping to the local gate is gradually increased by introducing a pump voltage (v_p) from a function generator. We pump the device at $2f_1$ using RF pump voltage, starting from 10mV to 170mV, and record the corresponding noise spectral density near the resonance. Figure 10a-10g show a series of thermomechanical noise spectra measured at various pump voltages. The voltage domain noise spectral density is converted to the displacement domain using the responsivity of the system and the measurement bandwidth. At low v_p, the thermomechanical noise spectrum slowly starts to increase with increasing pump strength. When v_p approaches the threshold pump voltage (v_t), the thermomechanical resonance shows giant amplification with exceptional spectral linewidth narrowing. Parametric pumping below v_t can be described by the equation

$$G = \frac{S_{x,\text{pump}}^{1/2}(\omega_1)}{S_x^{1/2}(\omega_1)} = \sqrt{1+\left(\frac{v_p^2}{v_t^2}\right)} \Big/ \left[1-\left(\frac{v_p^2}{v_t^2}\right)\right], \quad (8)$$

where G is the parametric gain [48] and $S_{x,\text{pump}}^{1/2}(\omega_1)$ and $S_x^{1/2}(\omega_1)$ are the spectral peak with and without parametric pumping. Fitting the data to Eq. (8), we obtain a parametric threshold voltage $v_t \approx 157$mV. From the data, we also estimate the critical gain $G_{crt} \approx 10{,}000$ (80dB).

The spectral linewidth narrowing is another appealing feature of parametric amplification since smaller linewidth of the resonance peak results in higher effective Q. Without parametric drive, the Q of the 1st mode is 274. The linewidth of noise spectral density drops sharply near v_t due to spectral narrowing. With $v_p = 153$mV, the linewidth narrowing factor (Δ_0/Δ_p) reaches ~5000, corresponding to effective or enhanced quality factor $Q_{eff} \approx 1.4 \times 10^6$. Here, Δ_0 and Δ_p are linewidth without and with pumping. We cannot reliably capture the linewidth narrowing beyond $v_p = 153$mV due to the 1Hz resolution bandwidth limit imposed by the instrument. When $v_p > 157$mV, the captured response of the resonator using the spectrum analyzer deviates from the simple harmonic resonator model and only shows a sharp single peak. We also sweep f_p with $v_p < v_t$ to observe the effect of f_p on parametric amplification. Sweeping f_p with fixed $v_p = 145$mV reveals a range for f_p that can parametrically pump the resonator [53], as shown in Fig. 10j with spectrum analyzer measurements. The response clearly shows the parametric amplification is higher when the f_p is near twice the fundamental resonance mode of the drumhead.

VIII. PHONONIC FREQUENCY COMB VIA 2:1 INTERNAL RESONANCE AND MODE COUPLING

The multimodal MoS_2 drumhead resonator exhibits a 3rd mode (Fig. 8e) that lies within the parametric pump range near $2f_1$. As we vary the pump frequency, the 2:1 internal resonance condition is satisfied between the 1st mode and the 3rd mode, leading to generation of PnFC. The essential governing equations describing the nonlinear mode coupling between mode 1 and mode 3 can be written as

$$m_{\text{eff},1}\ddot{x}_1 + m_{\text{eff},1}\omega_1\dot{x}_1/Q_1 + \left[k_{1,1} + k_p\cos(2\omega_1 t)\right]x_1 + k_{3,1}x_1^3 + 2\zeta x_1 x_3 = 0, \quad (9)$$

$$m_{\text{eff},3}\ddot{x}_3 + m_{\text{eff},3}\omega_3\dot{x}_3/Q_3 + k_{1,3}x_3 + k_{3,3}x_3^3 + \zeta x_1^2 = F(t), \quad (10)$$

where ζ is the nonlinear mode coupling between mode 1 and mode 3. The subscript 3 in Eq. (10) indicates the mode dependent parameters for mode 3. Figure 11a-11d show a series of measurements delineating the evolution of PnFC due to 2:1 internal resonance. As captured in careful spectrum analyzer

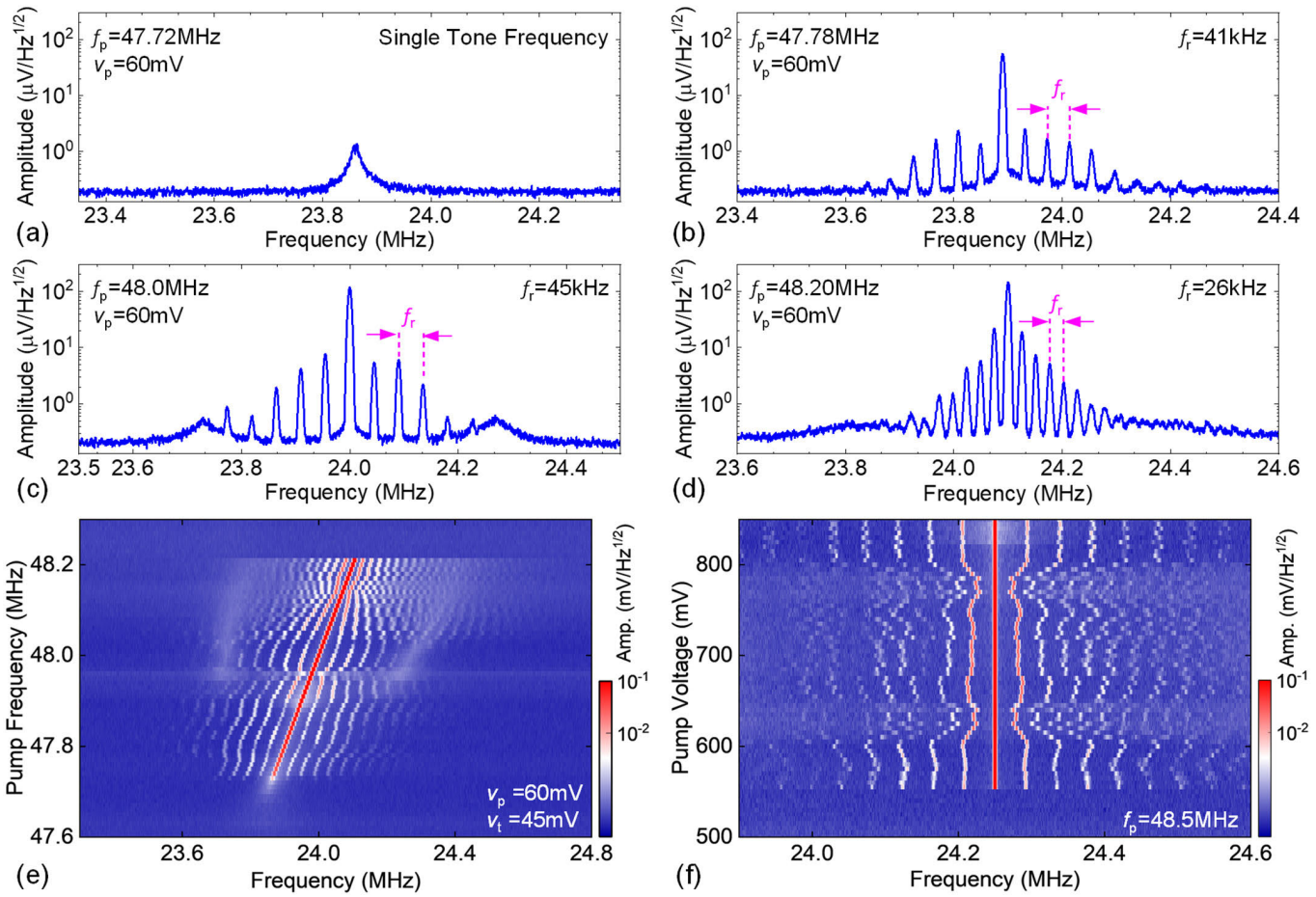

Fig. 11. Phononic frequency comb generation from 2:1 internal resonance and mode coupling. (a) Driving the device at $f_p = 47.72$MHz with $v_p = 60$mV generates a single tone frequency. (b) Increasing the drive frequency f_p to 47.78MHz breaks the single tone into multiple peaks and engenders phononic frequency comb structure with comb spacing $f_r \approx$41kHz. (c) Increasing the pump frequency f_p to 48.0MHz increases the comb spacing $f_r \approx$45kHz. (d) The comb spacing f_r reduces to 26kHz with $f_p = 48.2$MHz. (e) Evolution of phononic frequency comb structure with varying pump frequency with fixed $v_p = 60$mV with calibrated $v_t = 45$mV. (f) Characterization of phononic frequency comb with varying pump voltage with fixed pump frequency $f_p = 48.5$MHz. The threshold pump voltage goes up due to multiple measurement of the device with electrical parametric pumping.

measurements, pumping the device at $f_p = 47.72$MHz with $v_p = 60$mV only generates a single tone frequency. As we increase f_p to 47.78MHz, the single tone frequency breaks into multiple distinct peaks and form phononic frequency comb with comb spacing $f_r = 41$kHz. As we increase f_p to 48.0MHz, comb spacing increases to $f_r = 45$kHz, however, the number of comb teeth n_t decreases. As we further increase f_p to 48.2MHz, comb spacing decreases to $f_r = 26$kHz with increasing number of teeth. The PnFC disappears beyond $f_p =$ 48.22MHz.

Figure 11e depicts the evolution of the comb spacing and number of teeth with varying pump frequency in the single-layer MoS_2 NEMS resonator. Generated PnFC spacing can be tuned by controlling the pump strength v_p. Figure 11f shows the evolution of the PnFC with varying v_p with fixed $f_p = 48.5$MHz. The pump voltage for this measurement is significantly higher than Fig. 11e, possibly due to multiple measurements using electrical parametric amplification at different times and requires additional future study. Detailed comparison of our experimental results with existing literature is summarized in Table I. Our PnFC with 1:1 internal resonance exhibits comb spacing in the MHz regime, which are much larger than those in previously reported literature. The comb with 2:1 internal resonance displays comb spacing in the kHz regime with tunability. Therefore, utilizing the MoS_2 NEMS resonators, a wide range of comb spacing can be accessed via 1:1 and 2:1 internal resonances.

IX. Conclusion

In conclusion, we have experimentally demonstrated PnFC generation in atomically thin MoS_2 NEMS resonators by utilizing 1:1 and 2:1 mode coupling, achieved by the wide tunable range of the resonance frequency and exotic nonlinear dynamics in 2D MoS_2 membrane NEMS. PnFC responses are studied with various excitation and tuning parameters, including V_g, f_{drv}, and v_{drv}. The PnFC with 1:1 mode coupling demonstrates comb spacing f_r ~2.44MHz to 2.65MHz, whereas PnFC with 2:1 mode coupling exhibits comb structure with comb spacing f_r ~26kHz to 45kHz. Comparison between the PnFC responses and resonance behaviors, including frequency tuning and *DR*, suggests that the PnFC generation is related to 1:1 and 2:1 mode coupling and nonlinearity induced by the input driving signal. We have also demonstrated efficient electrical

parametric amplification by directly pumping the undriven thermomechanical noise response achieving giant parametric amplification up to ∼80dB and exceptional linewidth narrowing factor ∼5000. The findings here can contribute towards building high-performance and robust NEMS for sensing in classical and quantum applications.

REFERENCES

[1] T. W. Hänsch, "Nobel lecture: Passion for precision," *Rev. Mod. Phys.*, vol. 78, no. 4, pp. 1297–1309, Nov. 2006.

[2] S. A. Diddams, K. Vahala, and T. Udem, "Optical frequency combs: Coherently uniting the electromagnetic spectrum," *Science*, vol. 369, no. 6501, Jul. 2020, Art. no. eaay3676.

[3] R. Holzwarth, T. Udem, T. W. Hänsch, J. C. Knight, W. J. Wadsworth, and P. S. J. Russell, "Optical frequency synthesizer for precision spectroscopy," *Phys. Rev. Lett.*, vol. 85, no. 11, pp. 2264–2267, Sep. 2000.

[4] T. Udem, R. Holzwarth, and T. W. Hänsch, "Optical frequency metrology," *Nature*, vol. 416, no. 6877, pp. 233–237, 2002.

[5] L. Hollberg, S. Diddams, A. Bartels, T. Fortier, and K. Kim, "The measurement of optical frequencies," *Metrologia*, vol. 42, no. 3, pp. S105–S124, Jun. 2005.

[6] P. Del'Haye, A. Schliesser, O. Arcizet, T. Wilken, R. Holzwarth, and T. J. Kippenberg, "Optical frequency comb generation from a monolithic microresonator," *Nature*, vol. 450, no. 7173, pp. 1214–1217, Dec. 2007.

[7] T. J. Kippenberg, R. Holzwarth, and S. A. Diddams, "Microresonator-based optical frequency combs," *Science*, vol. 332, no. 6029, pp. 555–559, Apr. 2011.

[8] T. Fortier and E. Baumann, "20 years of developments in optical frequency comb technology and applications," *Commun. Phys.*, vol. 2, no. 1, p. 153, Dec. 2019.

[9] Q. Wang et al., "Dual-comb photothermal spectroscopy," *Nature Commun.*, vol. 13, no. 1, p. 2181, Apr. 2022.

[10] A. Erbe, H. Krömmer, A. Kraus, R. H. Blick, G. Corso, and K. Richter, "Mechanical mixing in nonlinear nanomechanical resonators," *Appl. Phys. Lett.*, vol. 77, no. 19, pp. 3102–3104, Nov. 2000.

[11] R. B. Karabalin, M. C. Cross, and M. L. Roukes, "Nonlinear dynamics and chaos in two coupled nanomechanical resonators," *Phys. Rev. B, Condens. Matter*, vol. 79, no. 16, Apr. 2009, Art. no. 165309.

[12] I. Mahboob, Q. Wilmart, K. Nishiguchi, A. Fujiwara, and H. Yamaguchi, "Tuneable electromechanical comb generation," *Appl. Phys. Lett.*, vol. 100, no. 11, Mar. 2012, Art. no. 113109.

[13] L. S. Cao, D. X. Qi, R. W. Peng, M. Wang, and P. Schmelcher, "Phononic frequency combs through nonlinear resonances," *Phys. Rev. Lett.*, vol. 112, no. 7, Feb. 2014, Art. no. 075505.

[14] A. Ganesan, C. Do, and A. Seshia, "Phononic frequency comb via intrinsic three-wave mixing," *Phys. Rev. Lett.*, vol. 118, no. 3, Jan. 2017, Art. no. 033903.

[15] A. Ganesan, C. Do, and A. Seshia, "Phononic frequency comb via three-mode parametric resonance," *Appl. Phys. Lett.*, vol. 112, no. 2, Jan. 2018, Art. no. 021906.

[16] D. A. Czaplewski et al., "Bifurcation generated mechanical frequency comb," *Phys. Rev. Lett.*, vol. 121, no. 24, Dec. 2018, Art. no. 244302.

[17] R. Wei et al., "A self-sustained frequency comb oscillator via tapping mode comb-drive resonator integrated with a feedback ASIC," in *Proc. IEEE 32nd Int. Conf. Micro Electro Mech. Syst. (MEMS)*, Jan. 2019, pp. 165–168.

[18] M. Park and A. Ansari, "Formation, evolution, and tuning of frequency combs in microelectromechanical resonators," *J. Microelectromech. Syst.*, vol. 28, no. 3, pp. 429–431, Jun. 2019.

[19] R. L. Kubena, W. S. Wall, J. Koehl, and R. J. Joyce, "Phononic comb generation in high-Q quartz resonators," *Appl. Phys. Lett.*, vol. 116, no. 5, Feb. 2020, Art. no. 053501.

[20] R. Singh et al., "Giant tunable mechanical nonlinearity in graphene-silicon nitride hybrid resonator," *Nano Lett.*, vol. 20, no. 6, pp. 4659–4666, Jun. 2020.

[21] Z. Qi, C. R. Menyuk, J. J. Gorman, and A. Ganesan, "Existence conditions for phononic frequency combs," *Appl. Phys. Lett.*, vol. 117, no. 18, Nov. 2020, Art. no. 183503.

[22] W. Luo, N. Gao, and D. Liu, "Multimode nonlinear coupling induced by internal resonance in a microcantilever resonator," *Nano Lett.*, vol. 21, no. 2, pp. 1062–1067, Jan. 2021.

[23] Q. Yang, L. Xu, R. Huan, Z. Jiang, A. Ganesan, and X. Wei, "Measurement of comb finger and comb spacing stability in phononic frequency comb," in *Proc. IEEE 16th Int. Conf. Nano/Micro Eng. Mol. Syst. (NEMS)*, Apr. 2021, pp. 1623–1626.

[24] A. Chiout et al., "Multi-order phononic frequency comb generation within a MoS_2 electromechanical resonator," *Appl. Phys. Lett.*, vol. 119, no. 17, Oct. 2021, Art. no. 173102.

[25] J. Lee, S. W. Shaw, and P. X.-L. Feng, "Phononic frequency comb generation via, 1:1 mode coupling in MoS_2 2D nanoelectromechanical resonators," in *Proc. 35th IEEE Int. Conf. Micro Electro Mech. Syst. (MEMS)*, Jan. 2022, pp. 503–506.

[26] X. Wang et al., "Frequency comb in 1:3 internal resonance of coupled micromechanical resonators," *Appl. Phys. Lett.*, vol. 120, no. 17, Apr. 2022, Art. no. 173506.

[27] A. Keşkekler, H. Arjmandi-Tash, P. G. Steeneken, and F. Alijani, "Symmetry-breaking-induced frequency combs in graphene resonators," *Nano Lett.*, vol. 22, no. 15, pp. 6048–6054, Aug. 2022.

[28] J. S. Ochs et al., "Frequency comb from a single driven nonlinear nanomechanical mode," *Phys. Rev. X*, vol. 12, no. 4, Nov. 2022, Art. no. 041019.

[29] J. Sun et al., "Generation and evolution of phononic frequency combs via coherent energy transfer between mechanical modes," *Phys. Rev. Appl.*, vol. 19, no. 1, Jan. 2023, Art. no. 014031.

[30] S M E. H. Yousuf, Y. Wang, J. Lee, S. W. Shaw, and P. X.-L. Feng, "Parametric amplification and phononic frequency comb generation in MoS_2 nanoelectromechanical resonators," in *Proc. 36th IEEE Int. Conf. Micro Electro Mech. Syst. (MEMS)*, Jan. 2023, pp. 613–616.

[31] G. Gobat, V. Zega, P. Fedeli, C. Touzé, and A. Frangi, "Frequency combs in a MEMS resonator featuring 1:2 internal resonance: *Ab initio* reduced order modelling and experimental validation," *Nonlinear Dyn.*, vol. 111, pp. 2991–3017, Feb. 2023.

[32] J. Lee, Z. Wang, K. He, J. Shan, and P. X.-L. Feng, "High frequency MoS_2 nanomechanical resonators," *ACS Nano*, vol. 7, no. 7, pp. 6086–6091, Jul. 2013.

[33] J. Lee, Z. Wang, K. He, R. Yang, J. Shan, and P. X.-L. Feng, "Electrically tunable single- and few-layer MoS_2 nanoelectromechanical systems with broad dynamic range," *Sci. Adv.*, vol. 4, no. 3, Mar. 2018, Art. no. eaao6653.

[34] T. Mei, J. Lee, Y. Xu, and P. X.-L. Feng, "Frequency tuning of graphene nanoelectromechanical resonators via electrostatic gating," *Micromachines*, vol. 9, no. 6, p. 312, Jun. 2018.

[35] F. Ye, A. Islam, T. Zhang, and P. X.-L. Feng, "Ultrawide frequency tuning of atomic layer van der Waals heterostructure electromechanical resonators," *Nano Lett.*, vol. 21, no. 13, pp. 5508–5515, Jul. 2021.

[36] B. Xu et al., "Nanomechanical resonators: Toward atomic scale," *ACS Nano*, vol. 16, no. 10, pp. 15545–15585, Oct. 2022.

[37] D. Rugar and P. Grütter, "Mechanical parametric amplification and thermomechanical noise squeezing," *Phys. Rev. Lett.*, vol. 67, no. 6, pp. 699–702, Aug. 1991.

[38] K. L. Turner, S. A. Miller, P. G. Hartwell, N. C. MacDonald, S. H. Strogatz, and S. G. Adams, "Five parametric resonances in a microelectromechanical system," *Nature*, vol. 396, pp. 149–152, Aug. 1998.

[39] I. Mahboob and H. Yamaguchi, "Bit storage and bit flip operations in an electromechanical oscillator," *Nature Nanotechnol.*, vol. 3, no. 5, pp. 275–279, Apr. 2008.

[40] R. B. Karabalin, X. L. Feng, and M. L. Roukes, "Parametric nanomechanical amplification at very high frequency," *Nano Lett.*, vol. 9, no. 9, pp. 3116–3123, Sep. 2009.

[41] J. Suh, M. D. LaHaye, P. M. Echternach, K. C. Schwab, and M. L. Roukes, "Parametric amplification and back-action noise squeezing by a qubit-coupled nanoresonator," *Nano Lett.*, vol. 10, no. 10, pp. 3990–3994, Oct. 2010.

[42] A. Eichler, J. Chaste, J. Moser, and A. Bachtold, "Parametric amplification and self-oscillation in a nanotube mechanical resonator," *Nano Lett.*, vol. 11, no. 7, pp. 2699–2703, Jul. 2011.

[43] P. Prasad, N. Arora, and A. K. Naik, "Parametric amplification in MoS_2 drum resonator," *Nanoscale*, vol. 9, no. 46, pp. 18299–18304, 2017.

[44] R. J. Dolleman, S. Houri, A. Chandrashekar, F. Alijani, H. S. J. van der Zant, and P. G. Steeneken, "Opto-thermally excited multimode parametric resonance in graphene membranes," *Sci. Rep.*, vol. 8, no. 1, p. 9366, Jun. 2018.

[45] R. Singh, R. J. T. Nicholl, K. I. Bolotin, and S. Ghosh, "Motion transduction with thermo-mechanically squeezed graphene resonator modes," *Nano Lett.*, vol. 18, no. 11, pp. 6719–6724, Nov. 2018.

[46] J. Lee, M. H. Matheny, M. L. Roukes, and P. X.-L. Feng, "AlN piezoelectric nanoelectromechanical isolator via parametric frequency conversion and amplification," in *Proc. 32nd IEEE Int. Conf. Micro Electro Mech. Syst. (MEMS)*, Jan. 2019, pp. 879–882.
[47] D. Bothner, S. Yanai, A. Iniguez-Rabago, M. Yuan, Y. M. Blanter, and G. A. Steele, "Cavity electromechanics with parametric mechanical driving," *Nature Commun.*, vol. 11, no. 1, p. 1589, Mar. 2020.
[48] J. Lee, S. W. Shaw, and P. X.-L. Feng, "Giant parametric amplification and spectral narrowing in atomically thin MoS_2 nanomechanical resonators," *Appl. Phys. Rev.*, vol. 9, no. 1, Mar. 2022, Art. no. 011404.
[49] C. Lee, H. Yan, L. E. Brus, T. F. Heinz, J. Hone, and S. Ryu, "Anomalous lattice vibrations of single- and few-layer MoS_2," *ACS Nano*, vol. 4, no. 5, pp. 2695–2700, May 2010.
[50] Z. Wang and P. X.-L. Feng, "Dynamic range of atomically thin vibrating nanomechanical resonators," *Appl. Phys. Lett.*, vol. 104, no. 10, Mar. 2014, Art. no. 103109.
[51] H. Jia et al., "Large-scale arrays of single- and few-layer MoS_2 nanomechanical resonators," *Nanoscale*, vol. 8, no. 20, pp. 10677–10685, 2016.
[52] T. Kaisar, J. Lee, D. Li, S. W. Shaw, and P. X.-L. Feng, "Nonlinear stiffness and nonlinear damping in atomically thin MoS_2 nanomechanical resonators," *Nano Lett.*, vol. 22, no. 24, pp. 9831–9838, Dec. 2022.
[53] J. M. L. Miller, D. D. Shin, H.-K. Kwon, S. W. Shaw, and T. W. Kenny, "Spectral narrowing of parametrically pumped thermomechanical noise," *Appl. Phys. Lett.*, vol. 117, no. 3, Jul. 2020, Art. no. 033504.
[54] B. Xu, J. Zhu, C. Jiao, J. Chen, and Z. Wang, "Atomically thin NEMS frequency comb with both frequency tunability and reconfigurable via simultaneous, 1:2 and 1:3 mode coupling," in *Proc. 36th IEEE Int. Conf. Micro Electro Mech. Syst. (MEMS)*, Jan. 2023, pp. 189–192.

S M Enamul Hoque Yousuf (Graduate Student Member, IEEE) received the B.S. degree in electrical and electronic engineering (EEE) from the Bangladesh University of Engineering and Technology (BUET) in 2017. He is currently pursuing the Ph.D. degree with the Department of Electrical and Computer Engineering (ECE), University of Florida (UF), Gainesville, FL, USA. His research interests include nano/microelectromechanical systems (NEMS/MEMS), atomic layer semiconductors and 2D devices, phononic frequency comb, and vibrating channel transistors. He was a recipient of the Margaret A. Ross Fellowship from ECE, UF, from 2020 to 2021, the Best Student Presentation Award from the AVS 2021 International Symposium, and one of the Outstanding Student Paper Award Finalist from the IEEE MEMS 2022 Conference.

Jaesung Lee (Member, IEEE) received the B.S. and M.S. degrees in electrical engineering from The University of Electro-Communications (UEC), Tokyo, Japan, and the Ph.D. degree in electrical engineering from Case Western Reserve University (CWRU) in 2017. He is currently an Assistant Professor with the Department of Electrical and Computer Engineering, The University of Texas at El Paso. His research interests have focused upon developing functional nanodevices (e.g., NEMS/MEMS, optoelectronic, and phononic devices) using advanced materials (e.g., 2D crystals and wide-bandgap semiconductors), toward building integrated systems for signal processing and sensing, in both classical and quantum regimes. He is the Co-Technical Program Chair for the MEMS/NEMS Technical Group from the 69th American Vacuum Society (AVS) International Symposium and Exhibition.

Steven W. Shaw received the A.B. degree in physics and the M.S.E. degree in applied mechanics from the University of Michigan, Ann Arbor, MI, USA, in 1978 and 1979, respectively, and the Ph.D. degree in theoretical and applied mechanics from Cornell University in 1983. He is currently a Professor of mechanical engineering with the Florida Institute of Technology, Melbourne, FL, USA, and the University Distinguished Professor Emeritus of mechanical engineering and an Adjunct Professor of physics and astronomy with Michigan State University, East Lansing, MI, USA. He has held regular or visiting appointments at Cornell University, Oakland University, the University of Michigan, Caltech, the University of Minnesota, the University of California-Santa Barbara, and McGill University. His research interests include micro/nano-scale resonators and vibration absorbers, with an emphasis on nonlinear behavior. He is a fellow of ASME. He was a recipient of the SAE Arch T. Colwell Merit Award, the Henry Ford Customer Satisfaction Award, the ASME Henry Hess Award, the ASME N. O. Myklestad Award, the ASME T. K. Caughey Dynamics Award, and the ASME J. P. Den Hartog Award.

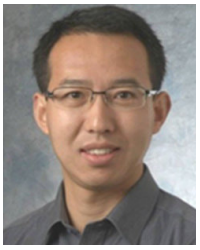

Philip X.-L. Feng (Senior Member, IEEE) received the Ph.D. degree in electrical engineering (EE) from the California Institute of Technology (Caltech), Pasadena, CA, USA, in 2007. He is currently a Professor with the Department of Electrical and Computer Engineering, University of Florida, Gainesville, Florida, USA. He has mentored/co-mentored 13 Ph.D. students to successful dissertation defense, mentored eight postdoctoral scholars, and also supervised 15 M.S. students. His research is primarily focused on emerging solid-state devices and systems, particularly nano/microelectromechanical systems (NEMS/MEMS), atomic layer semiconductors and 2D devices, silicon carbide (SiC) and other advanced semiconductors, quantum devices based on SiC and 2D materials, as well as their integration with state-of-the-art ICs and optical/photonic technologies. He was an invited participant to the National Academy of Engineering (NAE) U.S. Frontiers of Engineering (USFOE) Symposium in 2013 and subsequently a recipient of the NAE Grainger Foundation Frontiers of Engineering (FOE) Award in 2014. His awards also include the National Science Foundation CAREER Award in 2015 and the Presidential Early Career Award for Scientists and Engineers (PECASE) in 2019. He and his students has won six best paper/presentation awards from IEEE and other international conferences. He has served on the Technical Program Committees (TPCs) for the IEEE International Electron Devices Meeting (IEDM), the IEEE International Conference on Micro Electro Mechanical Systems (MEMS), International Conference on Solid-State Sensors, Actuators and Microsystems (Transducers), International Frequency Control Symposium (IFCS), IEEE SENSORS, and other international conferences. He served as a Track Chair for IEEE Sensors from 2016 to 2017, and the TPC Group four Chair for the IEEE IFCS from 2018 to 2020. He has also served as the Technical Program Chair for the MEMS/NEMS Technical Group from the 61st to 63rd American Vacuum Society (AVS) International Symposium and Exhibition. Since 2017, he has been a Co-Organizer and the Technical Chair of the SiC Materials and Devices Workshop. He has served as the Chair for the 34th IEEE International Conference on Micro Electro Mechanical Systems (IEEE MEMS 2021). He has also Co-Organized and Co-Chaired the Florida Semiconductor Week (FSW) Workshop in January 2023.